

SCIENTIFIC REPORTS

OPEN

Ultradispersed Cobalt Ferrite Nanoparticles Assembled in Graphene Aerogel for Continuous Photo-Fenton Reaction and Enhanced Lithium Storage Performance

Received: 04 April 2016

Accepted: 14 June 2016

Published: 04 July 2016

Bocheng Qiu, Yuanxin Deng, Mengmeng Du, Mingyang Xing & Jinlong Zhang

The Photo-Fenton reaction is an advanced technology to eliminate organic pollutants in environmental chemistry. Moreover, the conversion rate of $\text{Fe}^{3+}/\text{Fe}^{2+}$ and utilization rate of H_2O_2 are significant factors in Photo-Fenton reaction. In this work, we reported three dimensional (3D) hierarchical cobalt ferrite/graphene aerogels ($\text{CoFe}_2\text{O}_4/\text{GAs}$) composites by the *in situ* growing CoFe_2O_4 crystal seeds on the graphene oxide (GO) followed by the hydrothermal process. The resulting $\text{CoFe}_2\text{O}_4/\text{GAs}$ composites demonstrated 3D hierarchical pore structure with mesopores (14–18 nm), macropores (50–125 nm), and a remarkable surface area ($177.8 \text{ m}^2 \text{ g}^{-1}$). These properties endowed this hybrid with the high and recyclable Photo-Fenton activity for methyl orange pollutant degradation. More importantly, the $\text{CoFe}_2\text{O}_4/\text{GAs}$ composites can keep high Photo-Fenton activity in a wide pH. Besides, the $\text{CoFe}_2\text{O}_4/\text{GAs}$ composites also exhibited excellent cyclic performance and good rate capability. The 3D framework can not only effectively prevent the volume expansion and aggregation of CoFe_2O_4 nanoparticles during the charge/discharge processes for Lithium-ion batteries (LIBs), but also shorten lithium ions and electron diffusion length in 3D pathways. These results indicated a broaden application prospect of 3D-graphene based hybrids in wastewater treatment and energy storage.

Three dimensional (3D) graphene aerogels (GAs) with hierarchical porous structure have been attracting increasing attention in different fields, such as sensors^{1–3}, oil absorption^{4–6}, energy storage^{7–9}, and catalysis^{10,11}. These porous GAs not only inherit the intriguing properties of two-dimensional (2D) graphene sheet including excellent electrical conductivity and high surface area^{12–17}, but also endow graphene with controllable macro-appearance, high elastic property, adjustable porosity and ultralow density. More than these properties, the GAs building block can promote the separation of photogenerated electrons and holes, which can drastically enhance the performance of photocatalysts¹⁸. All these properties of GAs make it especially appealing as an ideal support to load various active components such as metal^{19,20}, metal sulfides²¹, and metal oxides^{22–24}. Recently, considerable efforts have been to devote to the development of 3D graphene-based composites for Lithium-ion batteries (LIBs) and catalysis^{25–28}. Huang *et al.* have pioneered the capture of SnO_2 into the 3D graphene frameworks by amphiphilic polymer-promoted assembly method and the resulting $\text{SnO}_2/\text{graphene}$ frameworks with controllable macroporous structures show the unprecedented high capacity and excellent cycle performance in LIBs²⁹. Our research group has reported a simple one-step hydrothermal method for the preparation of ultradispersed TiO_2 single nanocrystals grown *in situ* on the aerogel surface and the as-prepared TiO_2/GAs composites have highly recyclable photocatalytic activity, a high rate capability, and stable cycling in LIBs¹⁸. In order to extend the application of GAs in the environmental issues, the Fenton-reagent of $\text{Fe}_2\text{O}_3/\text{GAs}$ composites were successfully prepared

Key Laboratory for Advanced Materials and Institute of Fine Chemicals, East China University of Science and Technology, 130 Meilong Road, Shanghai 200237, P.R. China. Correspondence and requests for materials should be addressed to M.X. (email: mingyangxing@ecust.edu.cn) or J.Z. (email: jlzhang@ecust.edu.cn)

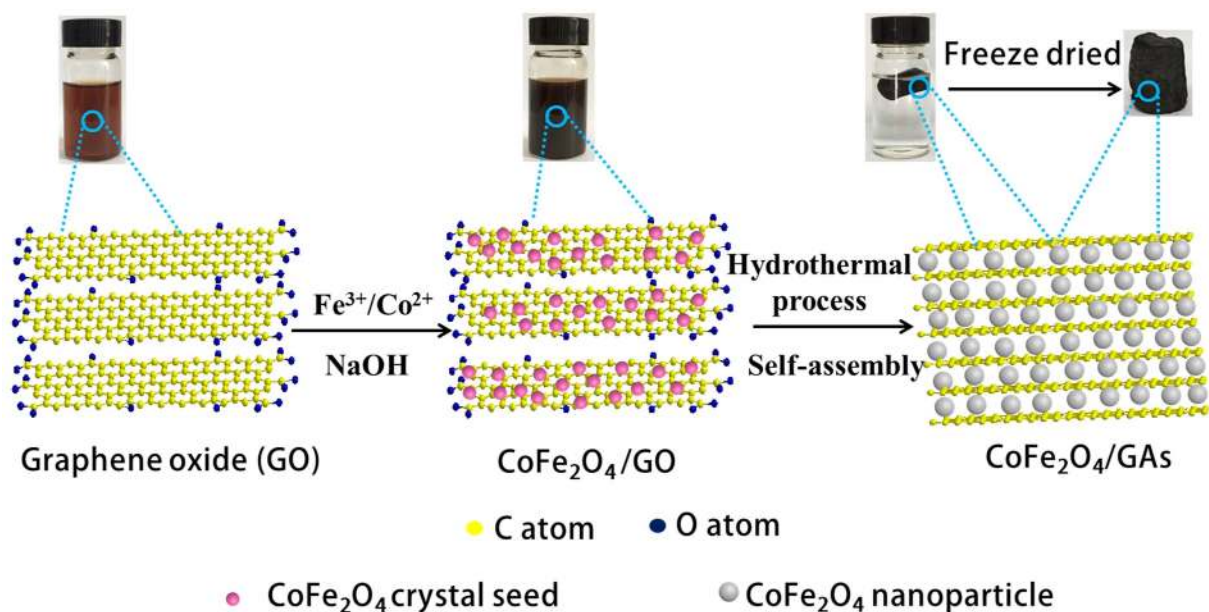


Figure 1. Fabrication process for CoFe₂O₄/GAs.

by a Stöber-like method, which displayed an ultrastable solar-driven Fenton activity over a wide pH range of 3.5–9.0³⁰. Different from above mentioned simple oxides, the composites based the mixed oxides and aerogels have been rarely reported. CoFe₂O₄ is a typical mixed oxide with potential Fenton-induced activity and Li⁺ storage property^{31–33}. On the other hand, CoFe₂O₄ as a kind of magnetic materials has been extensively studied due to its excellent chemical and mechanical stability³⁴, high coercive force³⁵, and potential applications in the fields of environment treatment³⁶, bioseparation and magnetic resonance imaging^{37,38}.

In this work, we employed a combined hydrothermal self-assembly and freeze-drying technology to construct the CoFe₂O₄/GAs composites with mesoporous and macroporous structure. Without any surfactant, ultradispersed CoFe₂O₄ nanoparticles and supporting 3D graphene network are simultaneously synthesized through a hydrothermal process using CoFe₂O₄ crystal seeds loaded on the surface of graphene oxide (GO) sheets as the basic building block. Compared with the mechanically mixed CoFe₂O₄/reduced graphene oxide (CoFe₂O₄/RGO) composites, the CoFe₂O₄/GAs composites demonstrate the 3D interconnected porous structure with a uniform deposition of CoFe₂O₄ nanoparticles, which can effectively capture electron to facilitate the Fe³⁺/Fe²⁺ conversion in Photo-Fenton reaction. Thereby, the CoFe₂O₄/GAs composites show a high Photo-Fenton activity for degradation of methyl orange pollutant. Besides, the 3D porous structure provides the short diffusion length, excellent conductive network and high surface area for lithium ions transport. As a result, the CoFe₂O₄/GAs composites exhibit excellent cyclic performance (830 mA h g⁻¹ for up to 50 charge/discharge cycles at a current density of 0.1 A g⁻¹) and good rate capability (830 and 340 mA h g⁻¹ at 0.1 and 2.0 A g⁻¹, respectively).

Results

The overall fabrication procedure of CoFe₂O₄/GAs is illustrated in Fig. 1. Firstly, iron nitrate hydrate (Fe(NO₃)₃•9H₂O) and cobalt nitrate hydrate (Co(NO₃)₂•6H₂O) are dissolved in the graphene oxide (GO) suspension at room temperature. During the process, positively charged Fe³⁺ and Co²⁺ can be absorbed to the hydroxyl and carboxyl groups on the surface of the negatively charged GO sheet by electrostatic attraction. The controllable nucleation site of CoFe₂O₄ on the GO sheet can be realized by the addition of sodium hydroxide (NaOH) solution. That is, upon the addition of NaOH solution, the hydrolysis of Fe³⁺ and Co²⁺ leads to the formation of CoFe₂O₄ crystal seeds deposited on the surface of GO sheets. This result can be confirmed by the HRTEM images of CoFe₂O₄/GO. As shown in Figure S1a,b, a large number of CoFe₂O₄ crystal seeds with a size of ~3 nm are highly dispersed on the GO sheets. Thereafter, the 2D GO sheets with a uniform decoration of CoFe₂O₄ crystal seeds self-assemble into the 3D monolithic networks during hydrothermal treatment, where reduction of GO sheets and crystallization and growth of CoFe₂O₄ crystal seeds are simultaneously realized. Finally, the CoFe₂O₄/GAs composites are obtained through the lyophilization. As a control experiment, the two-dimensional (2D) CoFe₂O₄/reduced graphene oxide (RGO) composites are prepared by physically mixing CoFe₂O₄ and RGO, denoted as CoFe₂O₄/RGO.

The morphology and microstructure of the resulting CoFe₂O₄/GAs composites were elucidated by scanning electron microscopy (SEM), field emission scanning electron microscopy (FESEM) and nitrogen adsorption/desorption analysis. As shown in Fig. 2a,b, the CoFe₂O₄/GAs composites show macroporous structure with well-defined interconnected pores at micrometer order. The partial overlapping or coalescence of the graphene sheet led to the physically cross-linked sites in the CoFe₂O₄/GAs composites. The driving force for assembly of 3D porous interconnected framework in CoFe₂O₄/GAs through the hydrothermal process should be ascribed to π-π interaction between graphene sheets. The FESEM images of CoFe₂O₄/GAs (Fig. 2c,d) exhibit that all the CoFe₂O₄

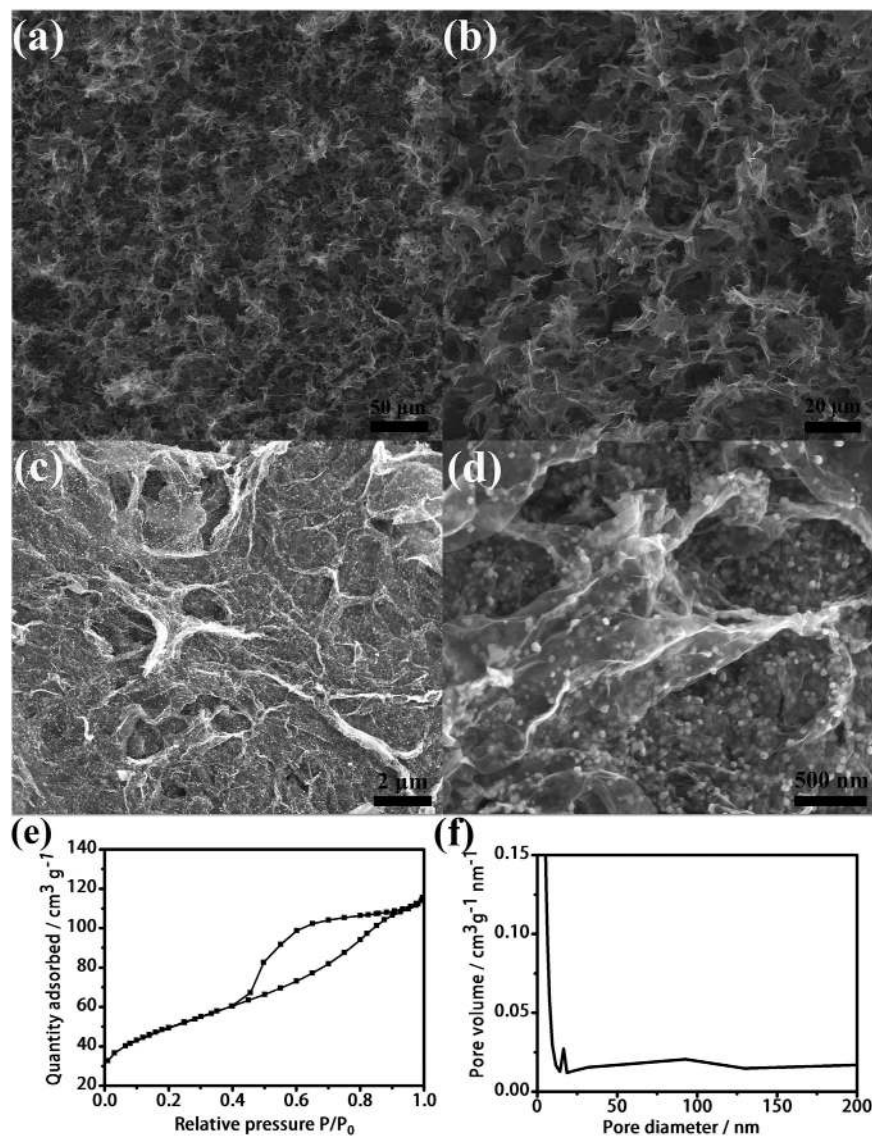


Figure 2. SEM and FESEM images. (a,b) SEM and (c,d) FESEM images of CoFe₂O₄/GAs. Nitrogen adsorption/desorption isotherms (e) and pore size distribution (f) of CoFe₂O₄/GAs.

nanoparticles with a size of around 9 nm are highly dispersed on the surface of RGO sheets. It is noteworthy that some CoFe₂O₄ nanoparticles can be encapsulated within the RGO sheets (Fig. 2d), which can effectively prevent the layer-by-layer stacking of GO sheets during the reduction process and avoid direct contact between CoFe₂O₄ and electrolyte. The mesoporous nature of the CoFe₂O₄/GAs composites was confirmed by nitrogen adsorption/desorption analysis. The adsorption data reveal a remarkably high specific surface area of 177.8 m²g⁻¹ (Fig. 2e), and the pore size distribution curve indicates the presence of hierarchical porous structure (Fig. 2f). The mesoporous size is in the range of 14–18 nm, and the macroporous size is in a wide range of 50–125 nm. This result highlights that the building up of 3D-GAs by hydrothermal method is an effective way to achieve a high surface area and hierarchical porous structure for 3D graphene-based materials.

TEM and HRTEM characterizations were conducted to obtain a closer morphology and structure of the CoFe₂O₄/GAs composites. The low-resolution TEM image (Fig. 3a) of the CoFe₂O₄/GAs composites exhibits that CoFe₂O₄ nanoparticles are uniformly deposited on the ultrathin RGO sheets, which is in good agreement with the FESEM result. Importantly, no obvious large and aggregated CoFe₂O₄ nanoparticles are visible, and no naked GO sheets or free CoFe₂O₄ nanoparticles appear. In addition, the TEM image (Fig. 3b) further reveals that a large number of CoFe₂O₄ nanoparticles are highly dispersed on the surface of RGO sheets. The size distribution curve of CoFe₂O₄ nanoparticles shows an average size focused on around 9 nm (Fig. 3b, inset). The HRTEM image (Fig. 3c) demonstrates that the highly crystalline CoFe₂O₄ nanoparticles are randomly distributed on two sides of RGO sheets with different contrasts. Moreover, the edge of RGO sheets can be clearly observed as indicated by the arrow (Fig. 3c) and some individual CoFe₂O₄ nanoparticles display clear crystal lattice with three kinds of spacing of 0.253 nm, 0.485 nm and 0.297 nm corresponding to the (311), (111) and (220) plane, respectively³¹.

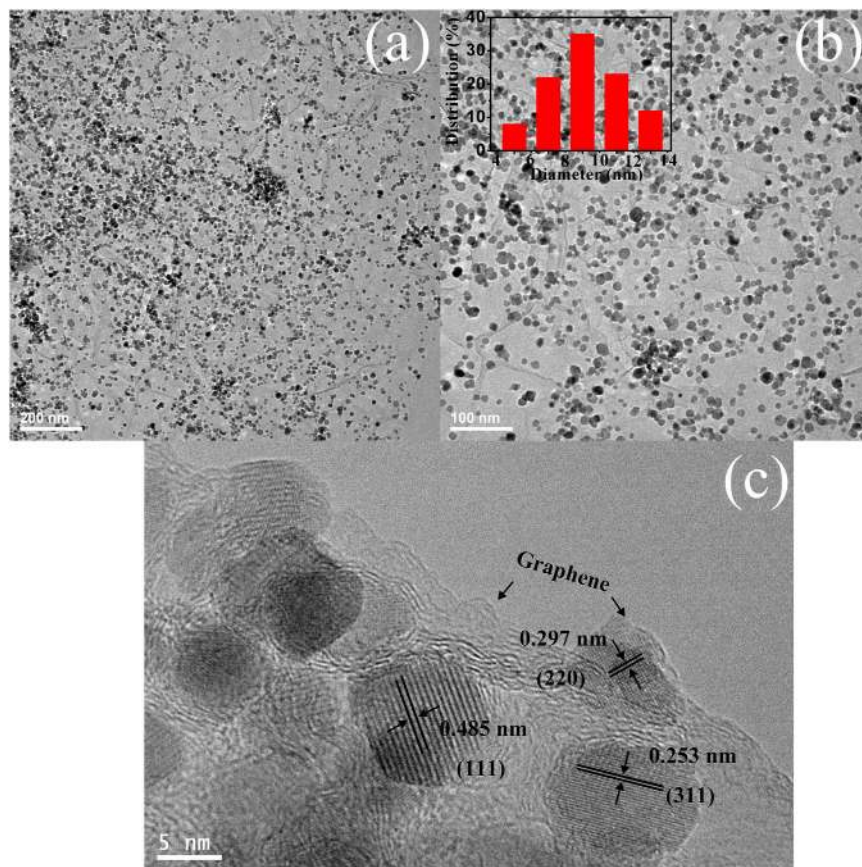


Figure 3. TEM and HRTEM images. (a,b) TEM images and (c) HRTEM image of CoFe₂O₄/GAs. Inset b is the corresponding particle size distribution of the loaded CoFe₂O₄ nanoparticles derived from 100 of CoFe₂O₄ particles in image (b).

Elemental mapping analysis of the CoFe₂O₄/GAs composites is performed to illustrate the distribution of carbon, cobalt, iron, and oxygen components in the composites (Figure S2). Apparently, the carbon, cobalt, iron, and oxygen components are uniformly distributed on RGO sheets, further verifying the ultradispersed distribution of CoFe₂O₄ nanoparticles on the surface of RGO sheets.

The XRD patterns of the as-prepared CoFe₂O₄/GAs depicted in Fig. 4a show diffraction peaks at $2\theta = 30.1^\circ$, 35.4° , 43.1° , 57.1° , 62.7° , which correspond to the crystal indexes of (220), (311), (400), (511), and (440) plane, respectively. All the diffraction peaks are completely consistent with the peaks of commercial CoFe₂O₄, indicating that the CoFe₂O₄ nanoparticles grown on the RGO sheets are well crystallized after the hydrothermal treatment. The presence of characteristic peaks in Raman spectra (Fig. 4b) also confirm the generation of highly crystallized CoFe₂O₄ on the RGO sheets. Moreover, the diffraction (001) reflection at $2\theta = 11.7^\circ$ of the initial GO sheet can be observed, but no corresponding diffraction peak can be observed in the XRD patterns of CoFe₂O₄/GAs, indicating the reduction of GO under the hydrothermal treatment. These results suggest the reduction of GO sheets and the crystallization of CoFe₂O₄ nanoparticles are proceed simultaneously. In addition, the obvious increase of the intensity ratio of D/G bands through the hydrothermal process in the Raman spectra further confirms the reduction of GO (D/G ratio increases from 0.96 to 1.03, Fig. 4b). TGA measurement carried out in the air was used to determine the mass fraction of CoFe₂O₄ in the composites. As shown in Fig. 4c, the TGA curve displays a significant weight loss at approximately 450 °C. The miniscule weight loss (<3%) that appeared below 300 °C is most likely attributed to the evaporation of water molecules adsorbed into the 3D interconnected networks. The major weight loss from 300 to 500 °C was about 20%, indicating the combustion of RGO. Therefore, the CoFe₂O₄/GAs composites contained about 72% (w/w) of CoFe₂O₄.

Discussion

The Fenton processes for waste water treatment have attracted more attention because of the formation of hydroxyl radicals ($\bullet\text{OH}$) during degradation³⁹. Actually, the generated $\bullet\text{OH}$ radicals are highly active and non-selective, and they are able to decompose many non-biodegradable and persistent organic compounds⁴⁰. Iron-containing materials⁴¹, other transitional metals⁴², or nonmetallic materials exhibit catalytic activity for the Fenton reaction. In addition, electro-, sono-, photo-assisted Fenton reaction, or to say, an integration technology, have been widely studied as well⁴³.

In this study, Photo-Fenton reactions are conducted for methyl orange (MO 10 mg/L) degradation to test the activity of CoFe₂O₄/GAs. The hydrochloric acid (HCl 0.1 M) is used to adjust the pH value of the reaction system.

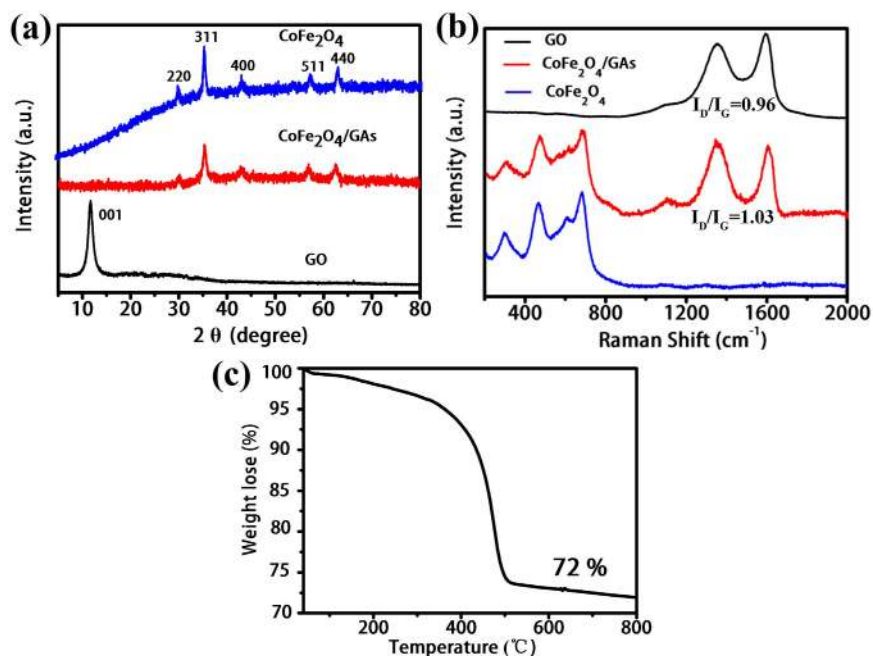


Figure 4. XRD patterns and TGA analysis. (a) XRD patterns of CoFe₂O₄, CoFe₂O₄/GAs and GO. (b) Raman spectra of GO, CoFe₂O₄/GAs and CoFe₂O₄. (c) Thermogravimetric analysis (TGA) curves of CoFe₂O₄/GAs composites in air from 40–800 °C with a heating rate of 20 °C min⁻¹.

The reaction is proceeded under the illumination of a 300 W Xenon lamp by an AM 1.5 G solar simulator. It is noteworthy, on the other hand, to highlight the fact that the CoFe₂O₄/GAs composites were grinded to powders in order to increase their contact area with the H₂O₂ molecules during the Photo-Fenton reaction, thereby improving the utilization efficiency of H₂O₂. As shown in Fig. 5a, the CoFe₂O₄/GAs composites in the dark show superior adsorption capacity in the first cycle test and all the MO molecules are adsorbed in 1 min. Thereafter, the adsorption capacity gradually decreased after 5 cycles, but 65% of the MO molecules can still be adsorbed in 30 min, which reveals the good adsorption capacity of CoFe₂O₄/GAs. With the addition of H₂O₂ in the dark, the decrement of MO content is caused by the adsorption and Fenton-like reaction. However, the Fenton-like reaction activity still decreased after 5 cycles, which suggests that the conversion efficiency of Fe³⁺/Fe²⁺ in the Fenton-like reaction without the aid of light is very low. So we introduce light into the Fenton-like reaction. As shown in Fig. 5a, the activity with photo-assisted has been improved greatly. Importantly, the activity keeps almost unchanged after 5 cycles, indicating the high conversion efficiency of Fe³⁺/Fe²⁺. For comparison, pure CoFe₂O₄ nanoparticles are prepared and keep a good dispersed state (Figure S3). Seen from Fig. 4a, pure CoFe₂O₄ shows decreased Photo-Fenton activity after 5 cycles due to low conversion efficiency of Fe³⁺/Fe²⁺ and leaching of Fe²⁺. Furthermore, we used 1, 10-phenanthroline monohydrate (Phen) as a testing Fe²⁺ reagent to detect the leaching of Fe²⁺ (Figure S4). The Fe²⁺ ions can react with the Phen to generate a strong visible absorption signal. After adding with Phen, the reaction solution of the CoFe₂O₄ powders gives a strong visible absorption signal, but the reaction solution of CoFe₂O₄/GAs gives a very low visible absorption signal, which indicates the leaching of Fe²⁺ ions in the aqueous solution is low. To further highlight the structure stability of CoFe₂O₄/GAs, we observe the morphology of the catalyst after 5 cycles. As shown in Figure S5, all the CoFe₂O₄ particles are still ultra-dispersed on the surface of RGO sheets (Figure S5a,b) and the 3D porous structure can be observed clearly (Figure S5c,d), which further reveals the high stability of structures. Figure S6 shows ferromagnetic property of the as-prepared CoFe₂O₄/GAs composites, suggesting that such composites might be easily separated from solution phase through inducing an external magnetic field.

The pH of the solution plays a key role in Photo-Fenton degradation of pollutants⁴⁴. The MO solution can be degraded with CoFe₂O₄/GAs within pH 3.5–9 (Fig. 5b). In order to excluding the strong adsorption of MO (Fig. 5a), we conducted cycle tests and selected the data of the third cycle test of CoFe₂O₄/GAs under different pH. It can be observed that the degradation rate decreases a little when pH is increased from 3.5 to 9, which is in good agreement with the previous reports^{30,45}. When pH is adjusted to 9, the Photo-Fenton degradation rate is up to 78% in 30 min. In addition, the H₂O₂ concentration on the rate of degradation of MO was also investigated by varying the H₂O₂ concentration from 25 to 150 mM (Fig. 5c). We also conducted cycle tests and selected the data of the third cycle test of CoFe₂O₄/GAs under different H₂O₂ concentration. Figure 5c shows the variation in the rate constants with H₂O₂ concentration in the presence of the catalyst. It can be seen that with the increasing of H₂O₂ concentration, the degradation rate of MO can be correspondingly improved. The enhanced Photo-Fenton activity is expected due to the increment of HO• yield from H₂O₂ reacted with Fe³⁺. Under a relative low H₂O₂ concentration (25 mM), all the MO molecules can be degraded in 30 min, exhibiting the high Photo-Fenton activity. Figure 5d demonstrates schematic representation of the Photo-Fenton reaction in the CoFe₂O₄/GAs composites. Firstly, the electron-hole pairs from CoFe₂O₄ are generated under simulated solar light irradiation (Eq. (1)).

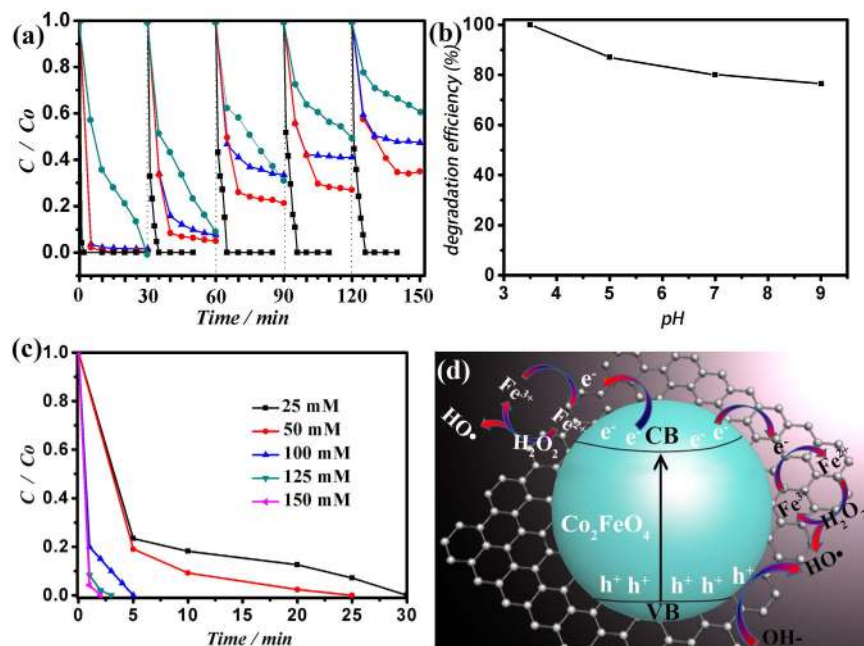
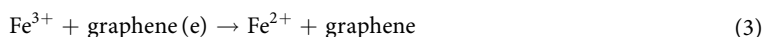
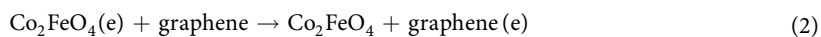


Figure 5. Photo-Fenton tests. Cycle test for the solar-driven degradation of methyl-orange (black line: $\text{CoFe}_2\text{O}_4/\text{GAs}$ with H_2O_2 under irradiation; red line: $\text{CoFe}_2\text{O}_4/\text{GAs}$ with H_2O_2 in the dark; blue line: $\text{CoFe}_2\text{O}_4/\text{GAs}$ without H_2O_2 in the dark; dark cyan line: pure CoFe_2O_4 powders with H_2O_2 under irradiation) (70 mL MO, 10 mg/L) under simulated solar light irradiation (with an AM 1.5 air mass filter) (150 mM H_2O_2 (30 wt%), the initial pH was 3.5) (a). Effect of solution pH on photodegradation efficiency of MO on $\text{CoFe}_2\text{O}_4/\text{GAs}$ photocatalyst (70 mL MO, 10 mg/L; 150 mM H_2O_2 (30 wt%); t:30 min; the third cycle data) (b). Effect of H_2O_2 concentration on photodegradation efficiency of MO on $\text{CoFe}_2\text{O}_4/\text{GAs}$ photocatalyst (70 mL MO, 10 mg/L; pH: 3.5; the third cycle data) (c). Photo-Fenton reaction mechanism of $\text{CoFe}_2\text{O}_4/\text{GAs}$ (d).

The photogenerated electrons are quickly trapped by graphene (Eq. (2)), limiting the recombination of holes and electrons. At the same time, the photogenerated holes (h^+) are subsequently trapped by OH^- to produce $\cdot\text{OH}$ radicals. The electrons trapped by graphene can be used to reduce Fe^{3+} to form Fe^{2+} (Eq. (3)). The Fe^{2+} can react with H_2O_2 to form $\cdot\text{OH}$ radical and Fe^{3+} (Eq. (4))³⁰. The generated Fe^{3+} can be reduced to Fe^{2+} again by the electron concentrated on the surface of RGO sheets to keep the cycle of $\text{Fe}^{3+}/\text{Fe}^{2+}$, thus achieving the high Photo-Fenton activity.



On the other hand, the lithium-insertion/extraction properties of the $\text{CoFe}_2\text{O}_4/\text{GAs}$ composites as anode material were investigated by galvanostatic charge/discharge measurements over a voltage range of 0.01–3.0 V. Figure 6a shows the charge/discharge curve of $\text{CoFe}_2\text{O}_4/\text{GAs}$ at a current density of 0.1 A g^{-1} . In the first discharge step, the $\text{CoFe}_2\text{O}_4/\text{GAs}$ composites present an extended/long voltage plateau at about 0.8 V, followed by a sloping curve down to the cut off voltage of 0.01 V, which is a typical characteristic of voltage trend for the CoFe_2O_4 electrode^{31,46}. A high initial reversible capacity of 1905 mA h g^{-1} can be derived in the first discharge step, with a corresponding charge capacity of 1037 mA h g^{-1} based on the weight of the $\text{CoFe}_2\text{O}_4/\text{GAs}$ composites. The initial capacity loss can be probably associated with the formation of solid electrolyte interphase (SEI) layer on the surface of electrode in the first discharge step⁴⁷. After 20 charge/discharge cycles, a high capacity of 830 mA h g^{-1} can still be retained. For comparison, the mechanically mixed $\text{CoFe}_2\text{O}_4/\text{RGO}$ composites were prepared (Figure S7). The mechanically mixed $\text{CoFe}_2\text{O}_4/\text{RGO}$ composites demonstrate a relatively low capacity of 1772 mA h g^{-1} , and the capacity decreases rapidly to 366 mA h g^{-1} after 20 charge/discharge cycles (Fig. 6b). In addition, the cycling performance of the $\text{CoFe}_2\text{O}_4/\text{GAs}$ composites is greatly superior to that of the mechanically mixed $\text{CoFe}_2\text{O}_4/\text{RGO}$ (Fig. 6c). The capacity of $\text{CoFe}_2\text{O}_4/\text{GAs}$ is very stable at the current density of 0.1 A g^{-1} and the high reversible capacity of 830 mA h g^{-1} is still retained after 50 cycles, while the capacity of $\text{CoFe}_2\text{O}_4/\text{RGO}$ rapidly decays from 1424 to 350 mA h g^{-1} . The rate performances of $\text{CoFe}_2\text{O}_4/\text{GAs}$ at the current rates of $0.1 \sim 2.0 \text{ A g}^{-1}$ are depicted in Fig. 6d. Reversible capacity are retained at 602 mA h g^{-1} and 500 mA h g^{-1} at 0.5 A g^{-1} and 1.0 A g^{-1} , respectively.

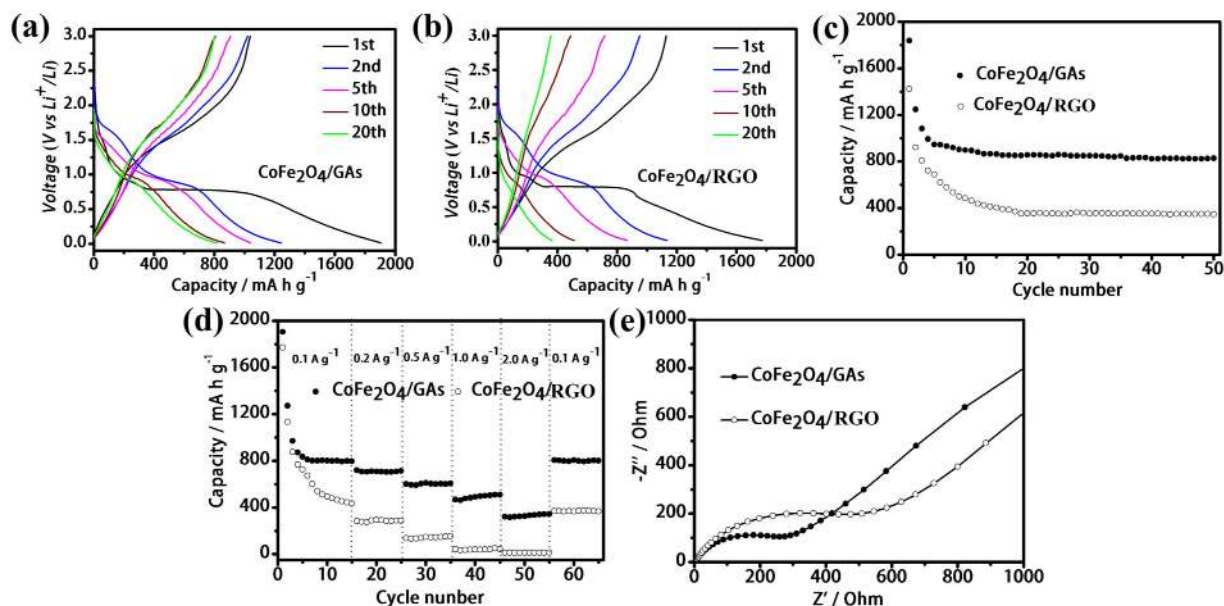


Figure 6. LIBs tests. The charge/discharge curves of $\text{CoFe}_2\text{O}_4/\text{GAS}$ (a) and mechanically mixed $\text{CoFe}_2\text{O}_4/\text{GR}$ (b) electrodes at constant current densities of 0.1 A g^{-1} . Cycling performance of $\text{CoFe}_2\text{O}_4/\text{GAS}$ composites and $\text{CoFe}_2\text{O}_4/\text{GR}$ composites electrode at constant current densities of 0.1 A g^{-1} (c). Rate capability of $\text{CoFe}_2\text{O}_4/\text{GAS}$ composites and $\text{CoFe}_2\text{O}_4/\text{RGO}$ composites at each current density between 0.1 and 2 A g^{-1} (d). Nyquist plots of the electrodes of $\text{CoFe}_2\text{O}_4/\text{GAS}$ and $\text{CoFe}_2\text{O}_4/\text{RGO}$ composites. All of the measurements were conducted using a voltage window of $0.01\text{--}3.0 \text{ V}$ (e).

Remarkably, a high reversible capacity of 340 mA h g^{-1} at a high rate of 2.0 A g^{-1} for the $\text{CoFe}_2\text{O}_4/\text{GAS}$ composites can be delivered. Importantly, after charge/discharge tests at the high density current, the capacity of $\text{CoFe}_2\text{O}_4/\text{GAS}$ can still return to the initial value, suggesting the high stability of $\text{CoFe}_2\text{O}_4/\text{GAS}$. As a comparison, the $\text{CoFe}_2\text{O}_4/\text{RGO}$ composites demonstrated a much lower capacity of 15 mA h g^{-1} at a high rate of 2.0 A g^{-1} owing to the weak connections between CoFe_2O_4 nanoparticles and RGO sheets and the absence of 3D interconnected network. Figure 6e compares the Nyquist plots of electrodes of $\text{CoFe}_2\text{O}_4/\text{GAS}$ and $\text{CoFe}_2\text{O}_4/\text{RGO}$. Apparently, the $\text{CoFe}_2\text{O}_4/\text{GAS}$ electrode shows a much lower resistance than the $\text{CoFe}_2\text{O}_4/\text{RGO}$ electrode ($291 \text{ Vs. } 538 \Omega$), which might be attributed to the excellent conductivity and electrochemical activity of $\text{CoFe}_2\text{O}_4/\text{GAS}$.

In order to further highlight advantage of $\text{CoFe}_2\text{O}_4/\text{GAS}$, we synthesized pure CoFe_2O_4 (Figure S3) and GAS (Figure S8) and tested their LIBs performance, respectively (Figure S9). The cycle stability of these three materials is given in Figure S9a. It can be observed that pure CoFe_2O_4 showed the low Li^+ storage ability and bad stability due to the volume expansion and contraction associated with Li^+ insertion/extraction during the charge/discharge processes. The GAS electrode gives an initial charge capacity of only 307 mA h g^{-1} , much lower than that of $\text{CoFe}_2\text{O}_4/\text{GAS}$ at the same current density and also lower than its theoretical value (372 mA h g^{-1}). The rate capability of $\text{CoFe}_2\text{O}_4/\text{GAS}$, pure CoFe_2O_4 and GAS is compared in Figure S9b. Compared with pure CoFe_2O_4 and GAS, the $\text{CoFe}_2\text{O}_4/\text{GAS}$ composites demonstrate a remarkably improved rate capability. The charge capacities of $\text{CoFe}_2\text{O}_4/\text{GAS}$ at $0.1, 0.2, 0.5, 1.0, 2.0 \text{ A g}^{-1}$ are $830, 710, 602, 500$ and 340 mA h g^{-1} , respectively, greatly higher than those of bare pure CoFe_2O_4 and GAS.

The outstanding electrochemical behavior of $\text{CoFe}_2\text{O}_4/\text{GAS}$ with high capacity, stable cycle performance and excellent rate capacity, can be assigned to the following factors: (1) the unique 3D interconnected structure of $\text{CoFe}_2\text{O}_4/\text{GAS}$, which consists of macro- and mesopores on the graphene network, can effectively reduce the diffusion length for both electron and Li^+ ions and provide multidimensional routes to facilitate the transport of electrons in the bulk electrode. (2) The large surface area of $\text{CoFe}_2\text{O}_4/\text{GAS}$ can greatly improve ion adsorption for Li^+ ions insertion/extraction during the charge/discharge process. (3) The strong coupling effect between CoFe_2O_4 and GAS can prevent large volume expansion/contraction and aggregation of CoFe_2O_4 nanoparticles associated with Li^+ ions insertion/extraction during the discharge/charge process.

In conclusion, we have fabricated the $\text{CoFe}_2\text{O}_4/\text{GAS}$ composites through a facile and cost-efficient hydrothermal self-assembly and freeze-drying two-step strategy. The generation of CoFe_2O_4 nanoparticles is accompanied with the reduction of GO under the hydrothermal condition and the obtained CoFe_2O_4 nanoparticles with diameters focused on around 9 nm are ultra-dispersed on the surface of RGO sheets. The $\text{CoFe}_2\text{O}_4/\text{GAS}$ composites exhibit the superior Photo-Fenton activity for the degradation of MO in an aqueous system due to improved adsorption toward pollutants and high conversion efficiency of $\text{Fe}^{3+}/\text{Fe}^{2+}$. In addition, the magnetic recyclable usability of the $\text{CoFe}_2\text{O}_4/\text{GAS}$ composites demonstrates over many successive reaction cycles. Besides of the promising application in Photo-Fenton reaction, the composites show excellent lithium storage performance with high reversible capacity and remarkable cyclic retention at each current density when used the anode material in LIBs. We believe that such multifunctional composites will have many potential practical applications in the

environmental protection and energy development. It is also expected that the involved preparation method can be easily adapted and extended as a general approach to other systems for the preparation of highly dispersed nanoparticles on graphene aerogels.

Method

Materials. All chemicals, including $\text{Fe}(\text{NO}_3)_3 \cdot 9\text{H}_2\text{O}$ (AR), $\text{Co}(\text{NO}_3)_2 \cdot 6\text{H}_2\text{O}$ (AR), NaOH (AR), H_2SO_4 (AR), NaNO_3 (AR), KMnO_4 (AR), H_2O_2 (AR), acetonitrile (AR), hydrochloric acid (HCl) and ethanol (AR) were used as received without any further purification. Graphite powders were purchased from Sigma-Aldrich (St. Louis, MO), and ultrapure water was used for all experiments.

Synthesis of Graphene Oxide (GO). Graphene oxide (GO) was synthesized from natural graphite powder using a modified Hummers method⁴⁸. Typically, 2 g graphite powders were added into a mixture of 50 mL H_2SO_4 and 1 g NaNO_3 . The solution was kept at 5 °C in an ice bath under vigorous stirring for 2 h. Thereafter, 6 g KMnO_4 was added slowly into the mixture while the temperature was kept from exceeding 5 °C, then the temperature of the system was heated up to 35 °C and maintained for 2 h. Afterwards, 80 mL of water was slowly added and then the mixture was heated to 98 °C for 1 h. 280 mL of water and 80 mL of 30% H_2O_2 were added to end the reaction, followed by 5% HCl and filtration. Finally, the wet graphene oxide was freeze-dried at -60 °C for 24 h.

Synthesis of the $\text{CoFe}_2\text{O}_4/\text{GAs}$ composites. In a typical experiment, 75 mg GO powders were dispersed a mixed solvent containing 75 mL ethanol and 25 mL acetonitrile in an ultrasound bath for 90 min. Thereafter, 0.48 g $\text{Fe}(\text{NO}_3)_3 \cdot 9\text{H}_2\text{O}$ and 0.173 g $\text{Co}(\text{NO}_3)_2 \cdot 6\text{H}_2\text{O}$ were added into the solution under the stirring for 1 h, then 1 mL of NaOH (0.1 M) solution was added into the above solution while stirring. After stirring for 1 h, the suspension was centrifuged and washed with ethanol and water. The as-prepared product was re-dispersed in 25 mL of water followed by an ultrasonic treatment, which was then transferred into a 50 mL autoclave, and kept at 180 °C for 12 h. The aerogels was treated by freeze-drying to obtain a three-dimensional $\text{CoFe}_2\text{O}_4/\text{GAs}$ composites. As a control experiment, two-dimensional (2D) $\text{CoFe}_2\text{O}_4/\text{reduced graphene oxide (RGO)}$ composites were prepared by physically mixing CoFe_2O_4 and RGO. With the absence of GO, the pure CoFe_2O_4 nanoparticles were prepared by the similar method of preparation of $\text{CoFe}_2\text{O}_4/\text{GAs}$. Pure GAs were prepared by hydrothermal treatment of GO solution.

Characterization. X-ray diffraction (XRD) patterns of all samples were collected in the range 10–80° (2 θ) using a RigakuD/MAX 2550 diffract meter (Cu K radiation, $\lambda = 1.5406 \text{ \AA}$), operated at 40 kV and 100 mA. The morphologies were characterized by transmission electron microscopy (TEM, JEM2000EX). The particle size distribution curve was derived from 100 CoFe_2O_4 nanoparticles. The surface morphologies were observed by scanning electron microscopy (TESCAN nova III) and field emission scanning electron microscopy (FESEM, NOVA NanoSEM450). Raman measurements were performed at room temperature using Raman microscopes (Renishaw, UK) under the excitation wavelength of 532 nm. BET surface area measurements were carried out by N_2 adsorption at 77 K using an ASAP2020 instrument. Thermogravimetric and differential thermal analyses were conducted on a Pyris Diamond TG/DTA (PerkinElmer) apparatus at a heating rate of 20 K min^{-1} from 40 to 800 °C in air flow.

Photo-Fenton Reaction. The photocatalytic activity of each catalyst was evaluated by in terms of the degradation of methyl-orange (MO, 10 mg/L). The $\text{CoFe}_2\text{O}_4/\text{GAs}$ powders were added into a 100 mL quartz reactor containing 75 mL MO solution. Prior to reaction, the initial pH value of the MO solution was adjusted to a certain pH value with 0.1 M HCl or 0.1 M NH_3 . Fenton reaction was initiated by adding a known concentration of H_2O_2 (a certain volume value, 30 wt %) to the solution. A 300 W Xe lamp (with AM 1.5 air mass filter) was used as a simulated solar light source. At the given time intervals, the analytical samples were taken from the mixture and immediately centrifuged before filtration through a 0.22 μm millipore filter to remove the photocatalysts. The filtrates were analyzed by recording variations in the absorption in UV-vis spectra of MO using a Cary 100 ultraviolet visible spectrometer. The leaching of Fe ions during reaction was analyzed using a Cary 100 ultraviolet visible spectrometer. In detail, a certain amount of solution was taken from the Photo-Fenton system. Next, a centrifuge separated the supernatant from the solution. And then, 1 mL 1, 10-phenanthroline monohydrate (0.5 wt%) as a testing Fe^{2+} reagent were added into 3 mL supernatant. After 15 minutes' standing, the levels of ferrous iron were examined by using a Cary 100 ultraviolet visible spectrometer.

Electrochemical Measurements. The electrochemical experiments were performed in coin-type cells. The working electrodes were prepared by mixing the hybrids, carbon black (Super-P), and poly-(vinyl difluoride) (PVDF) at a weight ratio of 80:10:10 to form slurry in N-methyl-2-pyrrolidinone (NMP), which was coated onto a copper foil (99.6%). Pure lithium foils were used as counter and reference electrodes. The electrolyte was consisted of a solution of LiPF_6 (1 M) in ethylene carbonate (EC)/dimethyl carbonate (DMC) (1:1, in weight percent). The cells were assembled in an Ar-filled glove box with the concentrations of moisture and oxygen below 1 ppm. The electrochemical performance was tested on a LAND CT2001A battery test system in the voltage range of 0.01–3.00 V versus Li^+/Li at room temperature.

References

- Nardecchia, S., Carriazo, D., Ferrer, M. L., Gutiérrez, M. C. & del Monte, F. Three dimensional macroporous architectures and aerogels built of carbon nanotubes and/or graphene: synthesis and applications. *Chem. Soc. Rev.* **42**, 794–830 (2013).
- Bai, H., Sheng, K., Zhang, P., Li, C. & Shi, G. Graphene oxide/conducting polymer composite hydrogels. *J. Mater. Chem.* **21**, 18653–18658 (2011).
- Li, L., He, S., Liu, M., Zhang, C. & Chen, W. Three-Dimensional Mesoporous Graphene Aerogel-Supported SnO_2 Nanocrystals for High-Performance NO_2 Gas Sensing at Low Temperature. *Anal. Chem.* **87**, 1638–1645 (2015).

4. Sun, H., Xu, Z. & Gao, C. Multifunctional, Ultra-Flyweight, Synergistically Assembled Carbon Aerogels. *Adv. Mater.* **25**, 2554–2560 (2013).
5. Cong, H.-P., Ren, X.-C., Wang, P. & Yu, S.-H. Macroscopic multifunctional graphene-based hydrogels and aerogels by a metal ion induced self-assembly process. *ACS Nano* **6**, 2693–2703 (2012).
6. Wu, Z. Y., Li, C., Liang, H. W., Chen, J. F. & Yu, S. H. Ultralight, Flexible, and Fire-Resistant Carbon Nanofiber Aerogels from Bacterial Cellulose. *Angew. Chem.* **125**, 2997–3001 (2013).
7. Zhang, X. *et al.* Mechanically strong and highly conductive graphene aerogel and its use as electrodes for electrochemical power sources. *J. Mater. Chem.* **21**, 6494–6497 (2011).
8. Worsley, M. A. *et al.* Synthesis of graphene aerogel with high electrical conductivity. *J. Am. Chem. Soc.* **132**, 14067–14069 (2010).
9. Hu, H., Zhao, Z., Wan, W., Gogotsi, Y. & Qiu, J. Ultralight and highly compressible graphene aerogels. *Adv. Mater.* **25**, 2219–2223 (2013).
10. Meng, F. *et al.* Alkali-treated graphene oxide as a solid base catalyst: synthesis and electrochemical capacitance of graphene/carbon composite aerogels. *J. Mater. Chem.* **21**, 18537–18539 (2011).
11. Wu, Z.-S. *et al.* 3D nitrogen-doped graphene aerogel-supported Fe₃O₄ nanoparticles as efficient electrocatalysts for the oxygen reduction reaction. *J. Am. Chem. Soc.* **134**, 9082–9085 (2012).
12. Li, X., Wang, X., Zhang, L., Lee, S. & Dai, H. Chemically derived, ultrasoft graphene nanoribbon semiconductors. *Science* **319**, 1229–1232 (2008).
13. Li, X. *et al.* Large-area synthesis of high-quality and uniform graphene films on copper foils. *Science* **324**, 1312–1314 (2009).
14. Xing, M., Fang, W., Yang, X., Tian, B. & Zhang, J. Highly-dispersed boron-doped graphene nanoribbons with enhanced conductivity and photocatalysis. *Chem. Commun.* **50**, 6637–6640 (2014).
15. Xing, M., Li, X. & Zhang, J. Synergistic effect on the visible light activity of Ti³⁺ doped TiO₂ nanorods/boron doped graphene composite. *Sci. Rep.* **4**, 5493–5499 (2014).
16. Zhang, L., Xi, Z., Xing, M. & Zhang, J. Effects of the preparation order of the ternary P25/GO/Pt hybrid photocatalysts on hydrogen production. *Int. J. Hydrogen Energy* **38**, 9169–9177 (2013).
17. Qiu, B. *et al.* Facile synthesis of the Ti³⁺ self-doped TiO₂-graphene nanosheet composites with enhanced photocatalysis. *Sci. Rep.* **5**, 8591–8596 (2015).
18. Qiu, B., Xing, M. & Zhang, J. Mesoporous TiO₂ nanocrystals grown *in situ* on graphene aerogels for high photocatalysis and lithium-ion batteries. *J. Am. Chem. Soc.* **136**, 5852–5855 (2014).
19. Liu, R. *et al.* An Interface-Induced Co-Assembly Approach Towards Ordered Mesoporous Carbon/Graphene Aerogel for High-Performance Supercapacitors. *Adv. Funct. Mater.* **25**, 526–533 (2014).
20. Wang, B., Yan, S. & Shi, Y. Direct electrochemical analysis of glucose oxidase on a graphene aerogel/gold nanoparticle hybrid for glucose biosensing. *J. Solid State Electrochem.* **19**, 307–314 (2014).
21. Jiang, X. *et al.* *In situ* assembly of graphene sheets-supported SnS₂ nanoplates into 3D macroporous aerogels for high-performance lithium ion batteries. *J. Power Sources* **237**, 178–186 (2013).
22. Wang, R., Xu, C., Sun, J., Gao, L. & Yao, H. Solvothermal-Induced 3D Macroscopic SnO₂/Nitrogen-Doped Graphene Aerogels for High Capacity and Long-Life Lithium Storage. *ACS Appl. Mater. Interfaces* **6**, 3427–3436 (2014).
23. Wang, R. *et al.* Solvothermal-Induced Self-Assembly of Fe₂O₃/GS Aerogels for High Li-Storage and Excellent Stability. *Small* **10**, 2260–2269 (2014).
24. Zhao, J. *et al.* Facile preparation of one-dimensional wrapping structure: graphene nanoscroll-wrapped of Fe₃O₄ nanoparticles and its application for lithium ion battery. *ACS Appl. Mater. Interfaces* **6**, 9890–9896 (2014).
25. Tan, C. *et al.* High-performance tin oxide-nitrogen doped graphene aerogel hybrids as anode materials for lithium-ion batteries. *J. Power Sources* **270**, 28–33 (2014).
26. Han, W. *et al.* Enhanced photocatalytic activities of three-dimensional graphene-based aerogel embedding TiO₂ nanoparticles and loading MoS₂ nanosheets as Co-catalyst. *Int. J. Hydrogen Energy* **39**, 19502–19512 (2014).
27. Han, S., Wang, J., Li, S., Wu, D. & Feng, X. Graphene aerogel supported Fe₃(PO₄)₄(OH)₃·H₂O microspheres as high performance cathode for lithium ion batteries. *J. Mater. Chem. A* **2**, 6174–6179 (2014).
28. Xiao, L. *et al.* Self-Assembled Fe₂O₃/Graphene Aerogel with High Lithium Storage Performance. *ACS Appl. Mater. Interfaces* **5**, 3764–3769 (2013).
29. Huang, Y. *et al.* Amphiphilic Polymer Promoted Assembly of Macroporous Graphene/SnO₂ Frameworks with Tunable Porosity for High-Performance Lithium Storage. *Small* **10**, 2226–2232 (2014).
30. Qiu, B., Xing, M. & Zhang, J. Stöber-like method to synthesize ultralight, porous, stretchable Fe₂O₃/graphene aerogels for excellent performance in photo-Fenton reaction and electrochemical capacitors. *J. Mater. Chem. A* **3**, 12820–12827 (2015).
31. Liu, S. *et al.* Self-assembly of a CoFe₂O₄/graphene sandwich by a controllable and general route: towards a high-performance anode for Li-ion batteries. *J. Mater. Chem.* **22**, 19738–19743 (2012).
32. Lavela, P. *et al.* High-performance transition metal mixed oxides in conversion electrodes: a combined spectroscopic and electrochemical study. *J. Phys. Chem. C* **111**, 14238–14246 (2007).
33. Vidal-Abarca, C., Lavela, P. & Tirado, J. L. A ⁵⁷Fe Mössbauer spectroscopy study of cobalt ferrite conversion electrodes for Li-ion batteries. *J. Power Sources* **196**, 6978–6981 (2011).
34. Zheng, H. *et al.* Self-Assembled Growth of BiFeO₃-CoFe₂O₄ Nanostructures. *Adv. Mater.* **18**, 2747–2752 (2006).
35. Lee, J.-G., Park, J. Y., Oh, Y.-J. & Kim, C. S. Magnetic properties of CoFe₂O₄ thin films prepared by a sol-gel method. *J. Appl. Phys.* **84**, 2801–2804 (1998).
36. Ji, L. *et al.* One-pot preparation of graphene oxide magnetic nanocomposites for the removal of tetrabromobisphenol. *A. Fron. Env. Sci. Eng.* **7**, 442–450 (2013).
37. Li, N. *et al.* Preparation of magnetic CoFe₂O₄ functionalized graphene sheets via a facile hydrothermal method and their adsorption properties. *J. Solid State Chem.* **184**, 953–958 (2011).
38. Yao, Y. *et al.* Magnetic CoFe₂O₄-graphene hybrids: Facile synthesis, characterization, and catalytic properties. *Ind. Eng. Chem. Res.* **51**, 6044–6051 (2012).
39. Yang, X.-j., Xu, X.-m., Xu, J. & Han, Y.-f. Iron oxychloride (FeOCl): an efficient fenton-like catalyst for producing hydroxyl radicals in degradation of organic contaminants. *J. Am. Chem. Soc.* **135**, 16058–16061 (2013).
40. Xu, L. & Wang, J. Magnetic nanoscaled Fe₃O₄/CeO₂ composite as an efficient Fenton-like heterogeneous catalyst for degradation of 4-chlorophenol. *Environ. Sci. Technol.* **46**, 10145–10153 (2012).
41. Cui, Z.-M., Chen, Z., Cao, C.-Y., Jiang, L. & Song, W.-G. A yolk-shell structured Fe₂O₃@ mesoporous SiO₂ nanoreactor for enhanced activity as a Fenton catalyst in total oxidation of dyes. *Chem. Commun.* **49**, 2332–2334 (2013).
42. Navalon, S., de Miguel, M., Martin, R., Alvaro, M. & Garcia, H. Enhancement of the catalytic activity of supported gold nanoparticles for the Fenton reaction by light. *J. Am. Chem. Soc.* **133**, 2218–2226 (2011).
43. Chen, X. *et al.* Photocatalytic oxidation of organic pollutants catalyzed by an iron complex at biocompatible pH values: using O₂ as main oxidant in a Fenton-like reaction. *J. Phys. Chem. C* **115**, 4089–4095 (2011).
44. Al-Kahtani, A. A. & Abou Taleb, M. F. Photocatalytic degradation of Maxilon C.I. basic dye using CS/CoFe₂O₄/GONCs as a heterogeneous photo-Fenton catalyst prepared by gamma irradiation. *J. Hazard. Mater.* **309**, 10–19 (2016).
45. Sharma, R., Bansal, S. & Singhal, S. Tailoring the photo-Fenton activity of spinel ferrites (MFe₂O₄) by incorporating different cations (M = Cu, Zn, Ni and Co) in the structure. *RSC Adv.* **5**, 6006–6018 (2015).

46. Ding, Z., Yao, B., Feng, J. & Zhang, J. A facile nitrogen-doped carbon encapsulation of CoFe₂O₄ nanocrystalline for enhanced performance of lithium ion battery anodes. *J. Solid State Electrochem.* **18**, 19–27 (2014).
47. Huang, Y. *et al.* Assembly of Tin Oxide/Graphene Nanosheets into 3D Hierarchical Frameworks for High-Performance Lithium Storage. *ChemSusChem* **6**, 1510–1515 (2013).
48. Xing, M., Shen, F., Qiu, B. & Zhang, J. Highly-dispersed Boron-doped Graphene Nanosheets Loaded with TiO₂ Nanoparticles for Enhancing CO₂ Photoreduction. *Sci. Rep.* **4**, 6341–6347 (2014).

Acknowledgements

This work has been supported by the National Natural Science Foundation of China (21203062, 21173077, 21377038, 21237003, 21577036), the National Basic Research Program of China (973 Program, 2013CB632403), the Research Fund for the Doctoral Program of Higher Education (20120074130001), the Fundamental Research Funds for the Central Universities, and sponsored by “Chenguang Program” supported by Shanghai Education Development Foundation and Shanghai Municipal Education Commission (14CG30).

Author Contributions

M.X. and J.Z. conceived and designed the experiments. M.X. and B.Q. prepared the samples and performed characterization. B.Q., Y.D., M.D., M.X. and J.Z. were mainly responsible for preparing the manuscript. All the authors discussed the results and reviewed the manuscript.

Additional Information

Supplementary information accompanies this paper at <http://www.nature.com/srep>

Competing financial interests: The authors declare no competing financial interests.

How to cite this article: Qiu, B. *et al.* Ultradispersed Cobalt Ferrite Nanoparticles Assembled in Graphene Aerogel for Continuous Photo-Fenton Reaction and Enhanced Lithium Storage Performance. *Sci. Rep.* **6**, 29099; doi: 10.1038/srep29099 (2016).



This work is licensed under a Creative Commons Attribution 4.0 International License. The images or other third party material in this article are included in the article's Creative Commons license, unless indicated otherwise in the credit line; if the material is not included under the Creative Commons license, users will need to obtain permission from the license holder to reproduce the material. To view a copy of this license, visit <http://creativecommons.org/licenses/by/4.0/>